Effects of Lorentz Force and Gradient Force of Magnetic Field on the Seawater Corrosion Behavior of Carbon Steels

Haowei Huang, Huijuan Zhang,* Pengfei Li,* Yuebin Chen,* Shuanzhu Zhao,* Xiaotong Sun,* Hong-Guang Piao,‡,*** Xia Zhao,*** and Yanliang Huang‡,****

With the rapid development of modern civilization, the development of marine resources has become imminent, but seawater corrosion has become one of the most important factors hindering development. In order to overcome this problem, an environmentally friendly physical anticorrosion scheme based on a magnetic field ($\vec{B}$) has been proposed. In this context, we investigate the effect of the Lorentz force and gradient force of a magnetic field on the corrosion behavior of carbon steel in seawater. The experimental results show that the gradient force of a magnetic field inhibits corrosion while the Lorentz force promotes corrosion. Especially in the $\vec{B} \perp \vec{E}$ (corrosion electrical field) case, the Lorentz force influence on the corrosion behavior is greater than the gradient force, while in $\vec{B} \| \vec{E}$ case gradient force dominates. In addition, the effect mechanism of magnetic field on the corrosion behavior of carbon steel in seawater was revealed by comparison of corrosion product composition in different reaction regions and electrochemical impedance spectrum analysis, which will provide an experimental basis for the application of environmentally friendly marine anticorrosion technology based on a magnetic field.

KEY WORDS: carbon steels, electrochemical behaviors, magnetic field effects, seawater corrosion

INTRODUCTION

The development and utilization of marine resources is an important direction of current economic development.[1-3] Unlike the terrestrial environment, the marine environment is more complex. High concentrations of salt and abundant microorganisms[4-5] make seawater a highly corrosive electrolyte, which impacts metal corrosion more.[6] Carbon steel is widely used in marine engineering because of its high-cost performance in corrosion resistance. In recent years, it has been found that carbon steel, as a kind of soft magnetic material, has a great improvement in its corrosion resistance in seawater under the specific intervention of a magnetic field.[7-10] If the corrosion resistance of carbon steel can be improved by magnetic field intervention, it will provide a new anticorrosion solution for the future of marine engineering materials.

Metal corrosion refers to the process in which metal is gradually destroyed by chemical or electrochemical reactions with its environment. Its nature is a physical process in which electrons are directly transferred from metal atoms to other acceptors. Therefore, the corrosion behavior or process of a metal will be affected by a magnetic field or its own magnetization characteristics.[7,8,11-14] According to the magnetohydrodynamic (MHD), mass transport during electrochemical corrosion of metals under magnetic fields is controlled by the Lorentz force ($\vec{F}_L$). The Lorentz force affects the convection in the solution, changes the ion movement in the solution, causes the change of ion concentration near the electrode, and thus affects the mass transport process in the electrochemical corrosion reaction. It obeys the following relationship:[11,15]

$$\vec{F}_L = \vec{J} \times \vec{B} \quad (1)$$

where $\vec{J}$ is the flux density of the moving charged particles and $\vec{B}$ is the magnetic field. In addition to the $\vec{F}_L$, a magnetic field gradient force ($\vec{F}_B$)[16-17] can also be caused by the stray field around the magnetic material or the nonuniform distribution of the space $\vec{B}$. The $\vec{F}_B$ causes paramagnetic ions to be subjected to a translational force to gather on the carbon steel surface and cause adsorption, which can inhibit the convection in the corrosion reaction process, reduce the corrosion current density, and increase the density of corrosion products on the surface of carbon steel. It follows the relationship:[18]

$$\vec{F}_B = \frac{1}{2\mu_0} c\chi_m \vec{\nabla} B^2 \quad (2)$$

where χ_m is the molar susceptibility, c is the concentration of magnetic species, and μ_0 is the vacuum permeability. Although other $\vec{B}$-dependent forces (e.g., paramagnetic force and magnetic damping force[16]) also play a role in the electrochemical reaction under $\vec{B}$, their effect is completely negligible compared with the influence of $\vec{F}_L$ and $\vec{F}_B$ on the surface of magnetic materials or magnet poles at the microscopic scale.[19-20]

In the corrosion process of magnetic metals, the effects of $\vec{F}_L$ and $\vec{F}_B$ on electrochemical corrosion become particularly

Submitted for publication: January 5, 2023. Revised and accepted: April 17, 2023. Preprint available online: April 17, 2023, https://doi.org/10.5006/4285.
‡ Corresponding authors. E-mail: hgpiao@ybu.edu.cn; hyl@qdio.ac.cn.
* Hubei Engineering Research Center of Weak Magnetic-Field Detection, China Three Gorges University, Yichang, China, 443002.
** Department of Physics, College of Science, Yanbian University, Yanji, China, 133002.
*** CAS Key Laboratory of Marine Environmental Corrosion and Bio-fouling, Institute of Oceanology, Chinese Academy of Sciences, Qingdao, China, 266071.

ISSN 0010-9312 (print), 1938-159X (online)

significant and different. $\vec{F}_L$ increases the current density by accelerating the mass transport process on the corrosion surface,[21] while $\vec{F}_B$ inhibits the formation of convection in the corrosion process by gathering paramagnetic ions. In the actual corrosion process, the two forces are competitive and difficult to be effectively considered separately. Therefore, the specific mechanism of their respective effects on metal corrosion behavior is still unclear, which will directly affect the wide application of carbon steel in ocean engineering. Fortunately, when the $\vec{B}$ direction is perpendicular to the corrosion electric field ($\vec{B} \perp \vec{E}$), the effect of $\vec{F}_L$ becomes significant, while when the $\vec{B}$ direction is parallel to the corrosion electric field ($\vec{B} \| \vec{E}$), the effect of $\vec{F}_B$ becomes obvious.[7,22]

According to the dependence of $\vec{F}_L$ and $\vec{F}_B$ on the direction of $\vec{B}$, we have investigated the effect of the two forces on the seawater corrosion behavior of carbon steel by designing $\vec{B} \perp \vec{E}$ and $\vec{B} \| \vec{E}$ cases. Combining the results of electrochemical experiment, corrosion product composition, and impedance spectroscopy, the effect mechanism of $\vec{F}_L$ and $\vec{F}_B$ on the electrochemical corrosion behavior of carbon steel in seawater was revealed, which will provide a reference for the application of magnetic materials in marine anticorrosion engineering.

EXPERIMENTAL AND FINITE ELEMENT SIMULATIONS

2.1 | Preparation of Samples

The sample A3-Q235 carbon steel sheet is a standard corrosion test piece of 72.4 mm × 12 mm × 2 mm (99.95% purity, Yangzhou Xiangwei Machinery Co., Ltd., China). All test samples were cleaned with absolute ethanol and deionized water and then coated with epoxy resin (1:1 ratio of epoxy resin and polyamide resin). The 12 mm × 2 mm reaction window in the carbon steel sample was sanded with 600 grit sandpaper and then polished with 2000 grit and 3000 grit sandpaper. After polishing the reaction surface of the samples, the surfaces were cleaned with absolute ethanol and deionized water. The experimental procedure used artificial seawater as the solution, artificial seawater is made by blending artificial sea salt (Weifang Huanyu Salt Chemical Co., Ltd.) with deionized water. According to the configuration instructions provided by the merchant, the sea salt concentration was 30 g/L and the pH value was adjusted to 8.2 by 1 M NaOH. We found that the NaCl concentration in the artificial seawater was ~2.4% as measured by a high-precision salinity meter. Ultrasonic stirring was performed during the solution preparation and the solution was exposed to static air during the experiment.

An electromagnet (East Changing Technologies EM-3, China) was used in our experiment to create uniform external $\vec{B}$ of 40 mT, 60 mT, and 80 mT in the effective region of the sample. Considering the influence of gravity on corrosion products in the electrochemical reaction process,[23] the effective reaction windows for $\vec{B} \| \vec{E}$ and $\vec{B} \perp \vec{E}$ cases are made on the side of carbon steel sheet in our experiments, as schematically shown in Figures 1(a) and (b). The carbon steel sample was placed in the geometric center area of the 35 mm gap between the poles of the electromagnet, while the center of the effective reaction window of the sample is in the region of uniform external . Before all electrochemical measurements, the open-circuit potential of each sample was monitored at 1,800 s to ensure that the corrosion reaction on the sample surface reached a steady state.

2.2 | Electrochemical Experiments

In order to investigate the effect of $\vec{B}$ on the electrochemical corrosion behavior of carbon steel, the galvanostatic polarization curve, potentiostatic polarization curve,

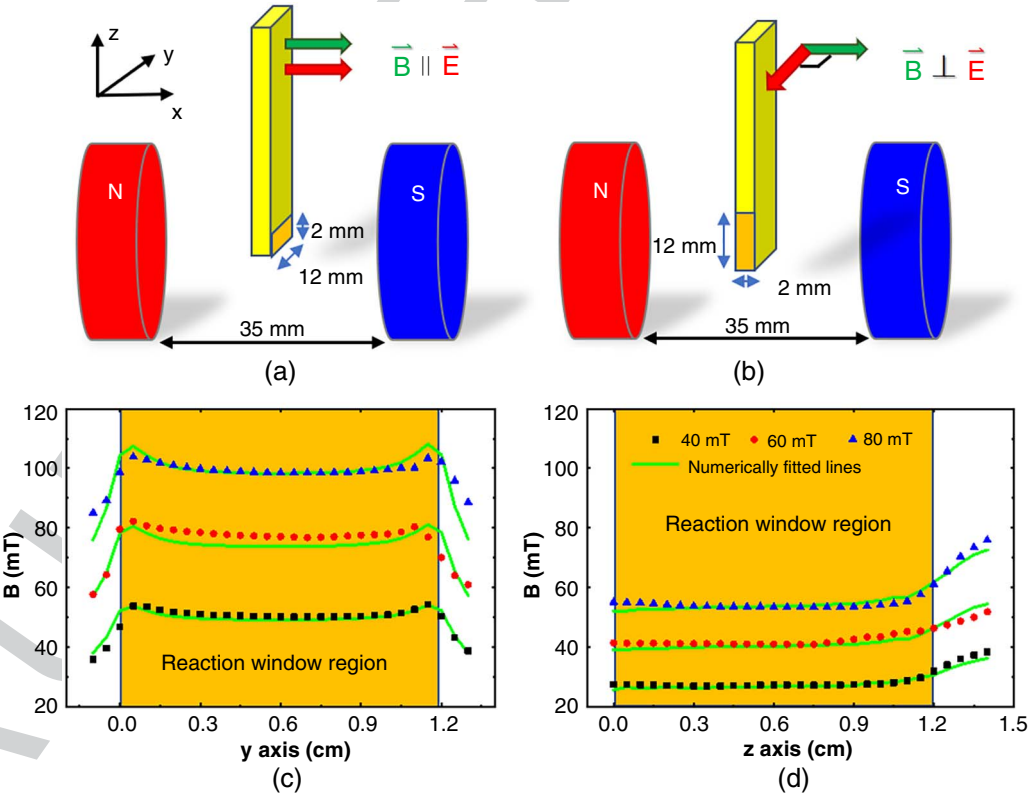

FIGURE 1. *Experimental schematics for (a) $\vec{B} \| \vec{E}$ and (b) $\vec{B} \perp \vec{E}$ cases; experimental measurement data and finite element simulation results on the $\vec{B}$ distribution on the corrosion window surface for (c) $\vec{B} \| \vec{E}$ and (d) $\vec{B} \perp \vec{E}$ cases under the different external $\vec{B}$ of 40 mT, 60 mT, and 80 mT.*

potentiodynamic polarization curve, and electrochemical impedance spectroscopy (EIS) were measured by using the three-electrode Teflon cell method under different $\vec{B}$. Here, electrochemical experiments and analyses were performed for both $\vec{B}||\vec{E}$ and $\vec{B} \perp \vec{E}$ cases using a Bipotentiostat (CH Instruments Ins. Model 760e†, China) by changing the $\vec{B}$ strength. In the three-electrode system of electrochemical experiments, a circular platinum electrode of 5 mm radius was used as a counter electrode, a saturated calomel electrode (SCE) as the reference electrode, and the reaction window of carbon steel samples as the working electrode. In quasi-steady state measurements of the galvanostatic polarization and potentiostatic polarization, the current density and constant potential were set to 0.02 A/cm^2 and −0.4 V_{SCE}, respectively. Potentiodynamic polarization curves were measured in the range of −0.45 V_{SCE} to −0.8 V_{SCE} with a scan rate of 5 mV/s based on an open-circuit potential. The EIS data were recorded from 10^5 Hz to 10^{-1} Hz with a 5 mV sinusoidal perturbing signal at the open-circuit potential. All experiment data were repeated more than three times to ensure the accuracy of the results.

2.3 | Characterizations of Morphology, Microstructure, and Magnetic Property

The corrosion surface morphology of the corroded surface of carbon steel samples formed under different $\vec{B}$ was characterized by the SEM (JEOL JSM-7500F†, Japan). The microstructure and chemical composition of corrosion products on carbon steel surface for $\vec{B}||\vec{E}$ and $\vec{B} \perp \vec{E}$ cases were characterized by the energy dispersive x-ray spectroscopy (EDS, Oxford† Instruments) equipped in the SEM and the x-ray powder diffraction (XRD, Rigaku Ultima IV†, Japan) with a conventional Cu-Kα radiation source. The physical property measurement system (Quantum Design VersaLab†, USA) was used to measure the magnetic property of the surface corrosion products.

2.4 | Measurement and Simulation for Magnetic Field Distribution

When the carbon steel sample was placed in the gap center between the two poles of the electromagnet, the $\vec{B}$ distributions in the longitudinal and transverse axes at 0.5 mm away from the sample surface were measured by using a high-precision Gauss meter (CH-Magnetoelectricity Technology CH-1800†, China), as shown in Figures 1(a) and (d). In order to verify the rationality of the $\vec{B}$ distribution measured in $\vec{B}||\vec{E}$ and $\vec{B} \perp \vec{E}$ cases, a finite element model was established according to the real size of the experiment, and the $\vec{B}$ distribution at 0.5 mm from the carbon steel surface was simulated, as shown in Figures 1(c) and (d).

RESULTS AND DISCUSSION

3.1 | Magnetic Field Distribution on Carbon Steel Surface

$\vec{F}_L$ and $\vec{F}_B$ are closely related to the $\vec{B}$ distribution on the surface of carbon steel because carbon steel is a magnetic material. For $\vec{B}||\vec{E}$ and $\vec{B} \perp \vec{E}$ cases, the nonuniform distribution of the → B (Surface magnetic induction intensity of carbon steel after magnetization) caused by the stray field around carbon steels was confirmed by the Gaussian meter and finite element simulations, as shown in Figures 1(c) and (d). The symbols and lines represent the experimental data and finite element simulation results, respectively. The actual $\vec{B}$ strength at the sample position is significantly enhanced by the carbon steel self-magnetization, and the distribution is not uniform due to the influence of the shape of carbon steel. In the $\vec{B}||\vec{E}$ case, with the external $\vec{B}$ increases, the $\vec{B}$ distribution on the surface of the corrosion window becomes more nonuniform, which is similar in the $\vec{B} \perp \vec{E}$ case. the corrosion windows are located in different parts of the carbon steel pattern in both cases, although the profiles of the $\vec{B}$ distributions are different, it can be seen that the $\vec{B}$ gradients at the edges or ends of the carbon steel are the most significant, which can be attributed to stray field contribution around carbon steel as a magnetic material.

3.2 | Polarization Measurements

Under the different external $\vec{B}$ of 0 mT, 40 mT, 60 mT, and 80 mT, the potentiodynamic polarization curves of carbon steels are measured for $\vec{B}||\vec{E}$ and $\vec{B} \perp \vec{E}$ cases, respectively shown in Figures 2(a) and (b). For the $\vec{B}||\vec{E}$ case, it can be seen that the profile difference of these curves under different external $\vec{B}$

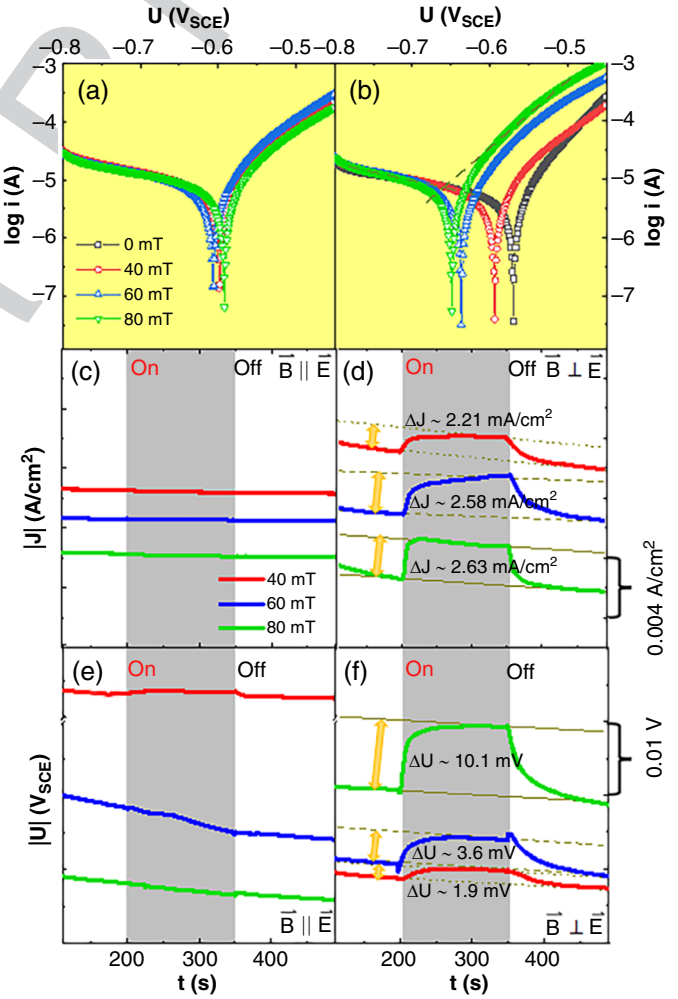

FIGURE 2. *Potentiodynamic polarization curves for (a) $\vec{B}||\vec{E}$ and (b) $\vec{B} \perp \vec{E}$ cases under different $\vec{B}$ strengths. Under the dynamically turn on/off of different strength $\vec{B}$, changes of the galvanostatic polarization curves with 0.02 A/cm^2 for (c) $\vec{B}||\vec{E}$ and (d) $\vec{B} \perp \vec{E}$ cases and the potentiostatic polarization curves with −0.4 V for (e) $\vec{B}||\vec{E}$ and (f) $\vec{B} \perp \vec{E}$ cases.*

† Trade name.

Table 1. *From Potentiodynamic Polarization Curves, the Corrosion Current (i), J and U Under Different $\vec{B}$ for the $\vec{B}\|\vec{E}$ and $\vec{B}\perp\vec{E}$ Cases were Obtained by Tafel Extrapolation Analysis*

	i (10^{-6} A)		J (10^{-5} A/cm^2)		U (V_{SCE})	
B (mT)	$\vec{B}\|\vec{E}$	$\vec{B}\perp\vec{E}$	$\vec{B}\|\vec{E}$	$\vec{B}\perp\vec{E}$	$\vec{B}\|\vec{E}$	$\vec{B}\perp\vec{E}$
0	7.516	4.808	3.132	2.003	−0.61	−0.571
40	7.447	5.834	3.103	2.431	−0.611	−0.605
60	7.379	6.95	3.075	2.896	−0.623	−0.653
80	7.244	7.08	3.018	2.95	−0.604	−0.67

strengths was not very significant, indicating that the external $\vec{B}$ has little effect on the corrosion of carbon steel in this case. However, for the $\vec{B}\perp\vec{E}$ case, the external $\vec{B}$ has a very significant effect on the corrosion behavior of carbon steel. From the Figure 2(b), it can be clearly seen that with the increase of the external $\vec{B}$ strength, the potentiodynamic polarization curve obviously shifts to the left. From the data in Table 1, for the $\vec{B}\|\vec{E}$ case, although the corrosion current density (J) and corrosion potential (U_{SCE}) hardly change much with the increase of the $\vec{B}$ strength, such as the changes under 80 mT are $\Delta J \approx 1.14$ μA/cm^2 and $\Delta U \approx 6$ mV, respectively relative to 0 mT, they still show a decreasing trend. In contrast, for the $\vec{B}\perp\vec{E}$ case, the changes of the J and U show a significant increasing trend with $\Delta J \approx 9.47$ μA/cm^2 and $\Delta U \approx 99$ mV under 80 mT relative to the $\vec{B}\|\vec{E}$ case, respectively. Here, if the J increases and the U_{SCE} becomes more negative, it means that corrosion is accelerated, while vice versa means that corrosion is inhibited. Therefore, our experimental results show that the $\vec{B}$ can promote the corrosion reaction of carbon steel in the $\vec{B}\perp\vec{E}$ case, while it can inhibit the corrosion in the $\vec{B}\|\vec{E}$ case.

In order to more intuitively reflect the effect of the $\vec{B}$ on the corrosion reaction of carbon steel in $\vec{B}\|\vec{E}$ and $\vec{B}\perp\vec{E}$ cases, the change of galvanostatic polarization and potentiostatic polarization curves was observed by dynamically manipulating $\vec{B}$ (the $\vec{B}$ turns on at 200 s and off at 350 s) at different strengths. For the $\vec{B}\|\vec{E}$ case, the dynamic turn on/off of different strengths $\vec{B}$ have no obvious effect on the potentiostatic polarization and galvanostatic polarization curves, as shown in Figures 2(c) and (e). Whereas in the $\vec{B}\perp\vec{E}$ case, the change of both curves is more significant, as shown in Figures 2(d) and (f). It is worth noting that the range of the change also shows an increasing trend with the increase of the external $\vec{B}$ strength, such as $\Delta J \approx 2.21$ mA/cm^2, 2.58 mA/cm^2, and 2.63 mA/cm^2 ($\Delta U \approx 1.9$ mV, 3.6 mV, and 10.1 mV) for 40 mT, 60 mT, and 80 mT, respectively. It can be observed that the above results are basically consistent with the result of the potentiodynamic polarization experiment.

3.3 | Characterizations of Morphology, Microstructure and Magnetic Property

In order to verify the different effect of $\vec{F}_B$ and $\vec{F}_L$ on surface corrosion of carbon steel under 40 mT, the corrosion surface morphology and the element composition of corrosion products after soaking 1,800 s in seawater were characterized on the middle (red line box) and edge (blue line box) parts of carbon steel samples with enlarged effective reaction area (12 mm × 6 mm, see Figure 3[a]) by SEM and EDS, respectively. As a reference sample, the corrosion surface morphology and element composition of the carbon steel sheet are characterized without the $\vec{B}$, as shown in Figure 3(b). It is observed that the surface morphology of the carbon steel sheet is relatively flat, but the content of oxygen (O) element is up to ~30%, which indicates that the surface can be corroded uniformly in the absence of the external $\vec{B}$. In contrast, the corrosion surface of carbon steel sheet becomes more coarse and uneven under 40 mT (see morphologies in Figure 3[c]), especially for the $\vec{B}\perp\vec{E}$ case, the O content of the surface corrosion products exceeds approximately 40% (see EDS data in FIGURE 3[c]). However, the difference between the middle (~42%, see the red line box) and edge (~41%, blue line box) parts of the effective corrosion surface is not obvious (~1%) in the $\vec{B}\perp\vec{E}$ case, which means that the $\vec{B}$ can significantly promote the corrosion of carbon steel in the $\vec{F}_L$ form.[7,24-25] In the $\vec{B}\|\vec{E}$ case, it is interestingly found that the O content difference between the middle (red line box) and edge (blue line box) parts of the effective corrosion surface becomes significant. According to the EDS data in Figure 3(d), the oxygen content of the middle part (~43%) in the corroded surface is much higher than that of the edge part (~19%) by ~24%, which obviously means that the action of the $\vec{B}$ is very different in the two parts. As carbon steel is a magnetic material, there will be stray fields around it under the external $\vec{B}$, which will lead to the formation of nonuniform $\vec{B}$ gradient regions at the two edges of the effective corrosion window of the carbon steel sheet, as shown in Figures 1(c) and (d). Therefore, the difference in O content between the middle and the edge parts should be caused by the difference of $\vec{B}$ gradient.[7,26-27] The dynamic behavior of magnetic ions in corrosive solution must be bound by the gradient force under gradient $\vec{B}$, which leads to the orientation of their behavior, that is, moving or converging along the direction of $\vec{B}$ gradient force.

In order to further confirm the existence of this behavior, the magnetic properties of original corrosion products on the surface of carbon steel were measured and their composition was also analyzed. As shown in the hysteresis loop in Figure 3(e), it is found that the corrosion products on the surface of carbon steel in the original state show the magnetic characteristics of typical magnetic materials. In addition, by comparing the morphology of the middle and edge parts of the corrosion surface of carbon steel in Figure 3(d), it can be observed that the corrosion surface at the edge is obviously denser and flatter. Obviously, it can be testified that dense corrosion products are formed on the surface of carbon steel under the action of $\vec{B}$ gradient force, which further inhibits the development of surface corrosion behavior.

To further confirm the chemical composition of the original corrosion product on the carbon steel surface, the XRD spectrum was used to analyze the corrosion product and was found to contain mainly FeOOH and NaCl (from the corrosion solution), as illustrated in Figure 3(f). Moreover, from the ratio of the overall signal intensity of FeOOH and NaCl, it can be observed that the proportion of FeOOH content in the corrosion products in the $\vec{B}\|\vec{E}$ case is significantly reduced compared with that in the $\vec{B}\perp\vec{E}$ case, which also indirectly

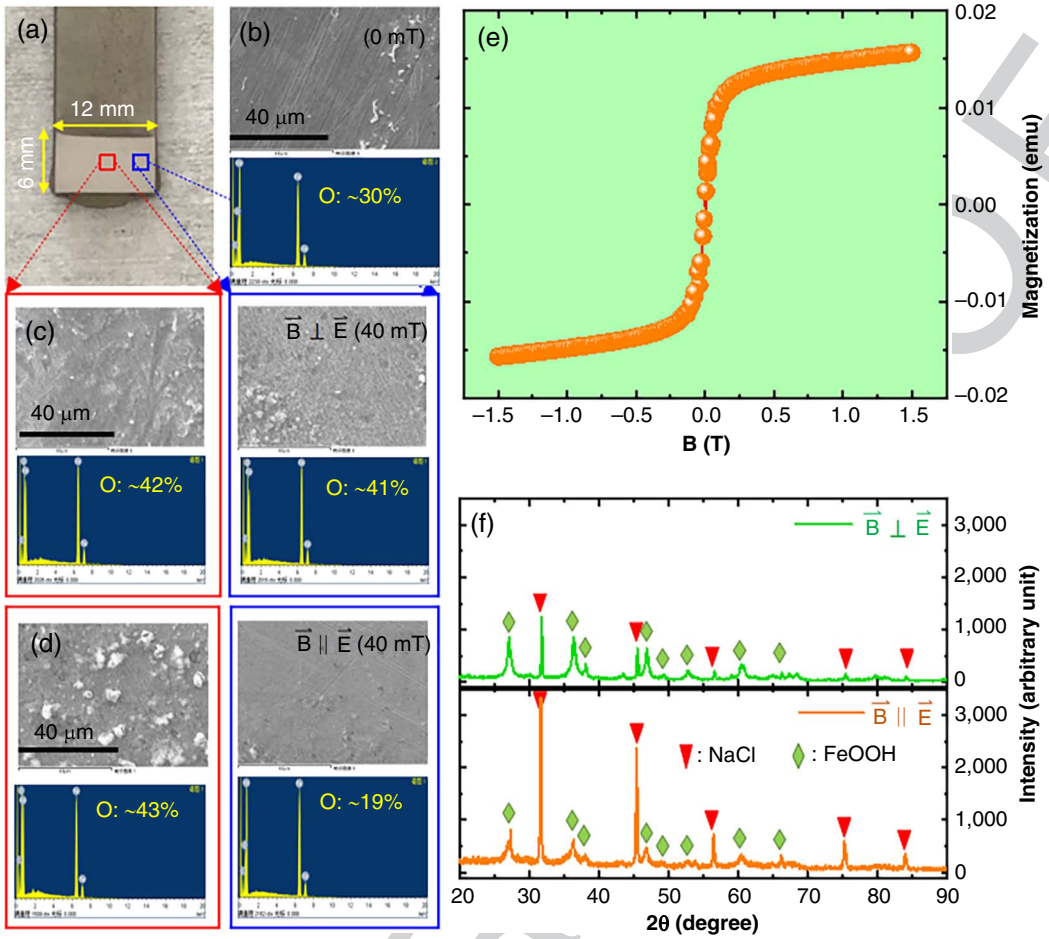

FIGURE 3. *(a) Shows the actual sample picture, where the red box represents the middle part of the corroded surface and the blue box represents the edge part. (b) Show the morphology and elemental composition (mainly O content) of the corroded surface of carbon steel without external* $\vec{B}$*. Under the 40 mT, (c) and (d) are shown the morphology and elemental composition at the middle and edge parts in the* $\vec{B} \perp \vec{E}$ *and* $\vec{B} \| \vec{E}$ *cases, separately. (e) The magnetic property of corrosion products is demonstrated by the hysteresis loop, and (f) the chemical composition of corrosion products for the* $\vec{B} \perp \vec{E}$ *and* $\vec{B} \| \vec{E}$ *cases are demonstrated by the XRD spectrum.*

indicates that the corrosion behavior of carbon steel in the $\vec{B} \| \vec{E}$ case is inhibited. The corrosion reaction process of carbon steel in seawater is usually considered as follows:[28-29]

$$Fe \rightarrow Fe^{2+} + 2e \quad (3)$$

$$Fe^{2+} \rightarrow Fe^{3+} + e \quad (4)$$

$$Fe^{3+} + 3OH^{-} \rightarrow FeOOH + H_2O \quad (5)$$

$$Fe^{2+} + 8FeOOH + 2e \rightarrow 3Fe_3O_4 + 4H_2O \quad (6)$$

$$3Fe_3O_4 + \frac{1}{2}O_2 \rightarrow 3Fe_2O_3 \quad (7)$$

To put it another way, the effect of $\vec{B}$ on the corrosion behavior of carbon steel is mainly reflected in the corrosion intermediates (FeOOH).

3.4 | Electrochemical Impedance Spectroscopy

In order to clarify the effect mechanism of the $\vec{B}$ on seawater corrosion of carbon steel, the EISs for the $\vec{B} \perp \vec{E}$ and $\vec{B} \| \vec{E}$ cases were carefully analyzed under the 0 mT, 40 mT, 60 mT, and 80 mT.

From the Nyquist plots in Figures 4(a) and (b), the capacitive rings can be observed at high frequency (see the blue-circled insets). This is due to the corrosion product FeOOH forming a porous, weakly adherent outer layer on the surface of the carbon steel.[8] From the Bode plots in Figures 4(c) and (d), it is also found that there were two times constants in the low- and middle-frequency regions, which is related to the effect of magnetic field on mass transport. The medium-frequency capacitive loop is a corrosion product formed in the solution due to the ferrous ions generated by the dissolution of the carbon steel, which exists between the iron oxide and the carbon steel.[30] The low-frequency region is the double-layer resistance to describe the process of charge transfer.[31-32] According to the chemical composition and morphology of surface corrosion products of carbon steel in seawater and the experience of other similar works, the equivalent circuit model $R_s(Q_{hf}(R_{hf}(Q_{mf}(R_{mf}(Q_{lf}R_{lf})))))$ of electrochemical corrosion was carefully constructed and depicted in the top inset of Figure 4(a). Castaneda and Benetton[30] also used an equivalent circuit with three times constants to fit the corrosion of carbon steel in artificial seawater, where the constant phase element (CPE) is

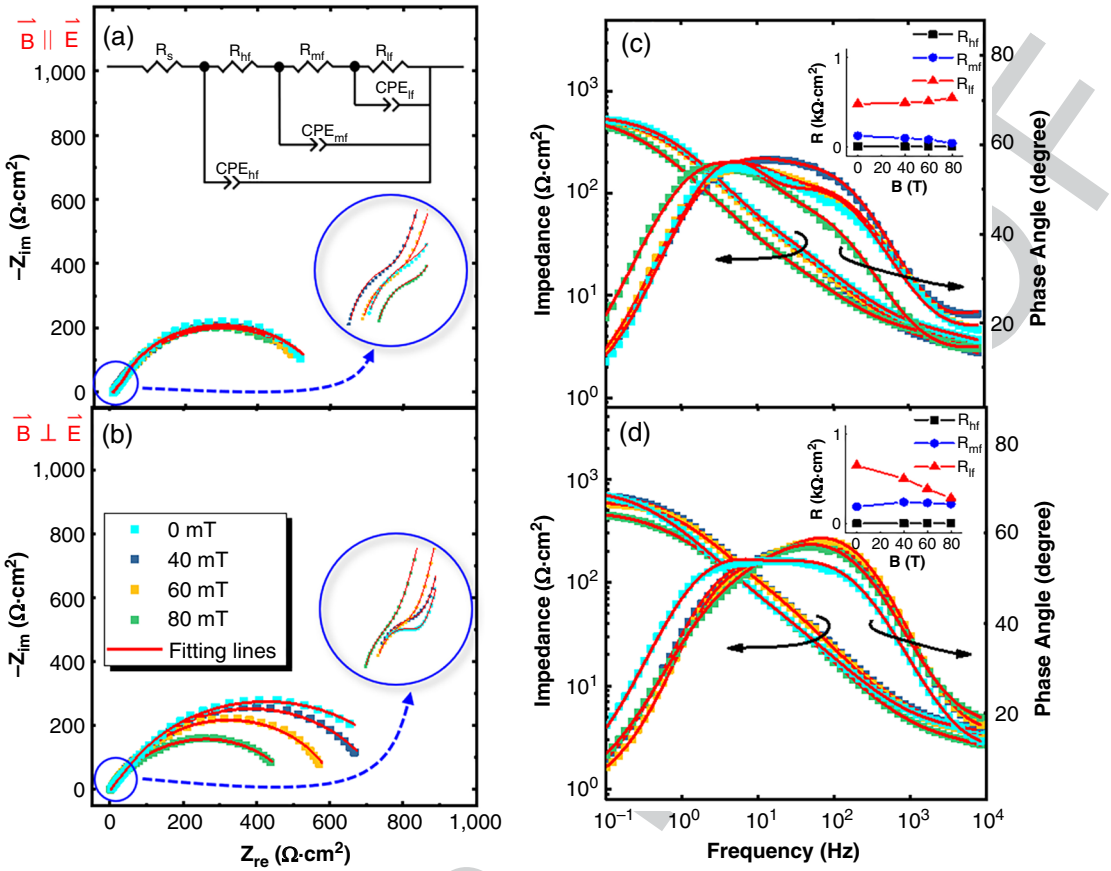

FIGURE 4. *Evolutions of Nyquist plots for (a) $\vec{B}||\vec{E}$ and (b) $\vec{B} \perp \vec{E}$ cases under different $\vec{B}$, the top inset of (a) shows the equivalent circuit model and the blue-circled insets of (a) and (b) are zooms in on the high-frequency regions. Evolutions of Bode plots for the (c) $\vec{B}||\vec{E}$ and (d) $\vec{B} \perp \vec{E}$ cases under different $\vec{B}$ and the insets show the variation trends of the R_{hf}, R_{mf}, and R_{lf} for the (a) $\vec{B}||\vec{E}$ and (b) $\vec{B} \perp \vec{E}$ cases with $\vec{B}$.*

Table 2. *Analysis Data of EISs for the $\vec{B}||\vec{E}$ and $\vec{B} \perp \vec{E}$ Cases under Different $\vec{B}$*

Cases	B (mT)	R_s ($\Omega \cdot cm^2$)	R_{hf} ($\Omega \cdot cm^2$)	Q_{hf}		R_{mf} ($\Omega \cdot cm^2$)	Q_{mf}		R_{lf} ($\Omega \cdot cm^2$)	Q_{lf}	
				Y_{hf} ($S^n\ \Omega^{-1} \cdot cm^{-2}$)	n_{hf}		Y_{mf} ($S^n\ \Omega^{-1} \cdot cm^{-2}$)	n_{mf}		Y_{lf} ($S^n\ \Omega^{-1} \cdot cm^{-2}$)	N_{lf}
$\vec{B}||\vec{E}$	0	1.864	2.926	6.28×10^{-5}	0.77	121.9	5.05×10^{-4}	0.73	477.1	1.27×10^{-4}	0.76
	40	1.371	2.244	2.80×10^{-5}	0.87	96.5	4.77×10^{-4}	0.77	494.2	2.58×10^{-4}	0.76
	60	1.728	2.351	6.10×10^{-5}	0.79	82.1	5.07×10^{-4}	0.74	507.6	2.32×10^{-4}	0.84
	80	2.259	2.12	6.72×10^{-5}	0.8	40.6	8.11×10^{-4}	0.74	545.8	4.35×10^{-4}	0.8
$\vec{B} \perp \vec{E}$	0	1.92	1.755	8.61×10^{-5}	0.87	186.9	5.11×10^{-4}	0.73	675.3	2.09×10^{-4}	0.83
	40	1.953	2.009	1.34×10^{-5}	0.86	239	2.86×10^{-4}	0.77	500.9	2.13×10^{-4}	0.81
	60	1.989	1.85	2.11×10^{-5}	0.86	229.8	2.64×10^{-4}	0.78	386.4	1.33×10^{-4}	0.86
	80	1.684	1.611	3.44×10^{-5}	0.87	217.1	4.49×10^{-4}	0.74	283.9	6.08×10^{-4}	0.7

used instead of the capacitor element to represent the inhomogeneity of the electrode surface.[33] The R_s denotes the solution resistance, R_{lf} denotes the charge transfer resistance, and Q_{lf} denotes the bilayer capacitance. The inner layer resistance and capacitance formed by ferrous ions are represented by R_{mf} and Q_{mf}, respectively. Similarly, the outer layer of resistors and capacitors formed by FeOOH is represented by R_{hf} and Q_{hf}, respectively. As shown in the red fitting lines of Figure 4, the constructed equivalent circuit model can well fit the impedance plots (evolutionary features and details of Nyquist plots and Bode plots) in the $\vec{B} \perp \vec{E}$ and $\vec{B}||\vec{E}$ cases, all of the EIS data are listed in Table 2. This means that the $\vec{B}$ application cannot change the overall reaction process of carbon steel corrosion, but only by controlling a certain corrosion link to promote or inhibit the corrosion of carbon steel.

For the case of $\vec{B}||\vec{E}$, it can be clearly seen that the radius of the two capacitance rings does not change significantly with the change of $\vec{B}$ intensity, as shown in Figure 4(a). However, for the case of $\vec{B} \perp \vec{E}$, a significant decrease in the radii of the two capacitance rings occurs with the increase of $\vec{B}$ intensity, as

shown in Figure 4(b). It is interesting to find that only the R_{lf} in these EIS data shows the most significant change under $\vec{B}$ and shows a monotone proportional response, as shown in the insets of Figures 4(b) and (c). With the increase of $\vec{B}$ intensity, the R_{lf} showed an obvious upward trend compared with R_{mf} and R_{hf} in the $\vec{B}\|\vec{E}$ case, such as the R_{lf} = 545.8 Ω·cm^2 at 80 mT which is about 13% higher than that at 0 mT. This means that the $\vec{B}$ enhancement ofbthe $\vec{B}\|\vec{E}$ case inhibits charge transfer during the corrosion of carbon steel. However, with the $\vec{B} \perp \vec{E}$ case, the R_{lf} showed a significant downward trend with the $\vec{B}$ intensity, such as the R_{lf} decreased about 58% when the $\vec{B}$ increases from 0 mT to 80 mT. This means that the $\vec{B}$ enhancement in the $\vec{B} \perp \vec{E}$ case clearly promotes charge transfer during the corrosion of carbon steel. This also corresponds to the increase of corrosion current in the above, showing the promotion of the corrosion reaction by the magnetic field in the case of $\vec{B} \perp \vec{E}$. Obviously, the above conclusions are completely consistent with the results of the potentiodynamic polarization experiments.

CONCLUSION

➢ The competitive relationship between $\vec{F}_L$ and $\vec{F}_B$ has been studied by changing the magnetic field direction for the corrosion behavior of carbon steel in seawater. Electrochemical methods were used to prove that $\vec{F}_L$ accelerates the corrosion reaction and $\vec{F}_B$ decelerates the corrosion reaction. Structural characterization verified the role of $\vec{F}_B$, and corrosion product analysis determined that the effect of the magnetic field influenced the corrosion intermediate product (FeOOH). EIS found that the magnetic field influenced the charge transfer of the reaction process to achieve the effect of changing the corrosion reaction. Although the experimental results show that the influence of $\vec{F}_L$ is significantly greater than that of $\vec{F}_B$ during the seawater corrosion of carbon steel, it is found that the $\vec{F}_B$ inhibition effect can be effectively utilized through experimental design. At present, magnetron corrosion protection is still not a viable alternative to existing corrosion protection solutions. but it is proved that the magnetic field gradient forces have a positive impact on electrochemical processes, and can provide a new idea for marine anticorrosion technology.

ACKNOWLEDGMENTS

This work was supported by the National Key R&D Program of China (Grants No. 2017YFB0903700 and 2017YFB0903702) and the Yanbian University Research Project (Grant No. 482022104). H.W. H. and H.J. Z. contributed equally to this work.

References

1. M. Visbeck, U. Kronfeld-Goharani, B. Neumann, W. Rickels, J. Schmidt, E. Doorn, N. Matz-Lück, A. Proelss, *Mar. Policy* 49 (2014): p. 87-89.
2. D. Ferrol-Schulte, P. Gorris, W. Baitoningsih, D.S. Adhuri, S.C.A. Ferse, *Mar. Policy* 52 (2015): p. 163-171.
3. Z. Wang, H. Lu, Z. Han, *Ocean Coast Manage.* 155 (2015): p. 60-67.
4. Y. Shen, Y. Dong, T. Liu, Z. Guo, Q. Li, L. Dong, Y. Yin, X. Wang, *Bioelectrochemistry* 132 (2020): p. 107408.
5. S. Agrawal, A. Adholeya, C.J. Barrow, S.K. Deshmukh, *Phytochem. Lett.* 23 (2018): p. 15-20.
6. S.A. Al-Fozan, A.U. Malik, *Desalination* 228 (2008): p. 61-67.
7. Y. Zhang, Y. Wang, S. Zhao, Y. Zhao, J. Zheng, X. Sun, H. Zhang, H.-G. Piao, Y. Huang, *Int. J. Electrochem. Sci.* 14 (2019): p. 11279-11288.
8. S. Zhao, Y. Wang, Y. Zhao, Y. Zhao, X. Sun, H. Zhang, H.-G. Piao, Y. Zhang, Y. Huang, *RSC Adv.* 10 (2020): p. 2060-2066.
9. S. Parapurath, A. Ravikumar, N. Vahdati, O. Shiryayev, *Appl. Sci.* 11 (2021): p. 9329.
10. Y. Yang, W. Ran, Q. Zhang, M. Sun, *Int. J. Electrochem. Sci.* 17 (2022): p. 220570.
11. H. Li, Q. Xiong, Z. Lu, J. Chen, Q. Xiao, X. Ru, S. Lin, J. Ma, Z. Chen, *Corros. Sci.* 129 (2017): p. 179-191.
12. M.E. Ghabashy, G.H. Sedahmed, I.A.S. Mansour, *Br. Corros. J.* 17 (1982): p. 36-37.
13. A. Ručinskien, G. Bikulčius, L. Gudavičiūt, E. Juzeliūnas, *Electrochem. Commun.* 4 (2002): p. 86-91.
14. J. Hu, C. Dong, X. Li, K. Xiao, *J. Mater. Sci. Technol.* 26 (2010): p. 355-361.
15. L.M. A. Monzon, J.M.D. Coey, *Electrochem. Commun.* 42 (2014): p. 38-41.
16. M. Waskaas, Y.I. Kharkats, *J. Phys. Chem. B* 103 (1999): p. 4876-4883.
17. G. Hinds, J.M.D. Coey, M.E.G. Lyons, *Electrochem. Commun.* 3 (2001): p. 215-218.
18. L.M.A. Monzon, J.M.D. Coey, *Electrochem. Commun.* 42 (2014): p. 42-45.
19. K.M. Grant, J.W. Hemmert, H.S. White, *Electrochem. Commun.* 1 (1999): p. 319-323.
20. S. Mohanta, T.Z. Fahidy, *J. Appl. Electrochem.* 8 (1978): p. 265-267.
21. X. Li, M. Zhang, B. Yuan, L. Li, C. Wang, *Electrochim. Acta* 222 (2016): p. 619-626.
22. R. Sueptitz, K. Tschulik, M. Uhlemann, L. Schhultz, A. Gebert, *Electrochim. Acta* 56 (2011): p. 5866-5871.
23. S. Wang, Y. Gu, Y. Geng, J. Liang, J. Zhao, J. Kang, *J. Alloys Compd.* 826 (2020): p. 153976.
24. L. Elias, A.C. Hegde, *J. Alloys Compd.* 712 (2017): p. 618-626.
25. A. Chiba, K. Kawazu, O. Nakano, T. Tamura, S. Yoshihara, E. Sato, *Corros. Sci.* 36 (1994): p. 539-543.
26. R. Sueptitz, K. Tschulik, M. Uhlemann, A. Gebert, L. Schultz, *Electrochim. Acta* 55 (2010): p. 5200-5203.
27. R. Sueptitz, K. Tschulik, M. Uhlemann, L. Schultz, A. Gebert, *Corros. Sci.* 53 (2011): p. 3222-3230.
28. Y. Ma, Y. Li, F. Wang, *Mater. Chem. Phys.* 112 (2008): p. 844-852.
29. K. Sugae, T. Kamimura, R. Asakura, T. Doi, H. Miyuki, T. Kudo, *Corros. Mater.* 70 (2019): p. 187-196.
30. H. Castaneda, X.D. Benetton, *Corros. Sci.* 50 (2008): p. 1169-1183.
31. S. Belkaid, M.A. Ladjouzi, S. Hamdani, *J. Solid State Electrochem.* 15 (2011): p. 525-537.
32. S.M. Bhola, S. Kundu, R. Bhola, B. Mishra, S. Chatterjee, *J. Mater. Sci.* 30 (2014): p. 163-171.
33. S.M. Bhola, R. Bhola, B. Mishra, D.L. Olsen, *J. Mater. Sci.* 45 (2010): p. 6179-6186.